SCA2026-037

Single-Phase Greyscale Lattice Boltzmann Simulation for Porous Media

Omid Tavakkoli[1], *Ying* Da Wang[2], *Benzhong* Zhao[3], *Peyman* Mostaghimi[1], *Zhe* Li[4,*] and *Ryan T.* Armstrong[1,*]

[1]School of Civil and Environmental Engineering, University of New South Wales, Sydney, Australia
[2]School of Minerals and Energy Resources Engineering, University of New South Wales, Sydney, Australia
[3]Department of Civil Engineering, McMaster University, Hamilton, Ontario, Canada
[4]The Australian National University, Research School of Physics, Canberra, 2601, Australia

Abstract. Pore-scale flow simulation in porous rocks traditionally requires binary segmentation of micro-CT images, discarding sub-voxel information and limiting the representable domain size. Here we present a greyscale lattice Boltzmann framework that operates directly on unsegmented images, treating each voxel as an effective porous medium characterised by a continuous porosity and a Kozeny–Carman permeability closure. We derive analytically that the framework recovers the Darcy–Brinkman equation under homogeneous porosity, and validate the heterogeneous extension against exact analytical and numerical benchmarks of increasing complexity. Applied to Bandera Brown sandstone, the framework reproduces high-resolution binary simulation results to within 1% on a co-registered sub-volume. At the full low-resolution domain scale, greyscale and binary simulations diverge by 93%, demonstrating that microporous voxels impose significant flow resistance that binary segmentation neglects. We further show that the Kozeny-Carman constant C scales as $\sqrt{C} \propto r$ with imaging resolution r, providing a practical approach when multi-resolution co-registered images are unavailable. This work establishes greyscale simulation as a practical and rigorous alternative to binary pore-scale modelling, particularly for rocks with multiscale porosity.

1 Introduction

Pore-scale simulation of flow in porous media has become a standard tool for predicting transport properties from three-dimensional images obtained via micro-computed tomography (micro-CT) [1, 2]. The prevailing workflow segments the grayscale image into a binary representation (pore or solid), and solves the governing equations directly on the resolved geometry, most commonly using the lattice Boltzmann method (LBM) [3, 4] or finite-volume Stokes solvers [5]. Pore-scale simulation has been applied successfully across a range of rock types and has demonstrated predictive capability for absolute permeability when the pore space is well resolved [6].

However, binary pore-scale modelling is subject to two fundamental limitations (Fig. 1). First, segmentation reduces a continuous field of X-ray attenuation values to a binary classification, discarding sub-voxel information. Voxels that contain a mixture of pore and solid in microporous regions, and in any geometry where the pore size approaches the imaging resolution are forced into one category or the other. The resulting permeability prediction is sensitive to the chosen segmentation threshold, introducing an often unquantified source of uncertainty [7, 8, 9]. Second, the requirement to fully resolve the pore space imposes a trade-off between resolution and field of view. Capturing the smallest pore throats demands high resolution, which in turn restricts the imaged volume and may compromise the representativity of the sample [10]. This limitation is particularly acute in rocks with multiscale porosity, such as carbonates, where macropores, microporous grains, and intermediate structures coexist across length scales that cannot be simultaneously resolved in a single image [11, 12].

Greyscale simulation addresses both limitations simultaneously. Rather than classifying each voxel as purely pore or solid, greyscale approaches assign a continuous porosity value to each voxel, representing the fraction of void space it contains. This allows flow simulation on unsegmented images, enabling larger and more representative computational domains while retaining information about unresolved pore-scale structure. The concept has been implemented within the lattice Boltzmann framework through two broadly distinct strategies. The first, introduced by [13], modifies the equilibrium distribution and collision operator to incorporate porosity and a porous drag force directly into the LBM evolution equation, recovering a volume-averaged form of the Navier–Stokes equations through the Chapman–Enskog procedure. The second employs partial bounce-back schemes, in which a fraction of the distribution functions at each node is reflected to mimic the resistance of unresolved solid structure [14, 15, 16]. Both approaches treat voxels as effective porous media rather than requiring binary classification, but they differ

* Corresponding author: zhe.li@anu.edu.au, ryan.armstrong@unsw.edu.au

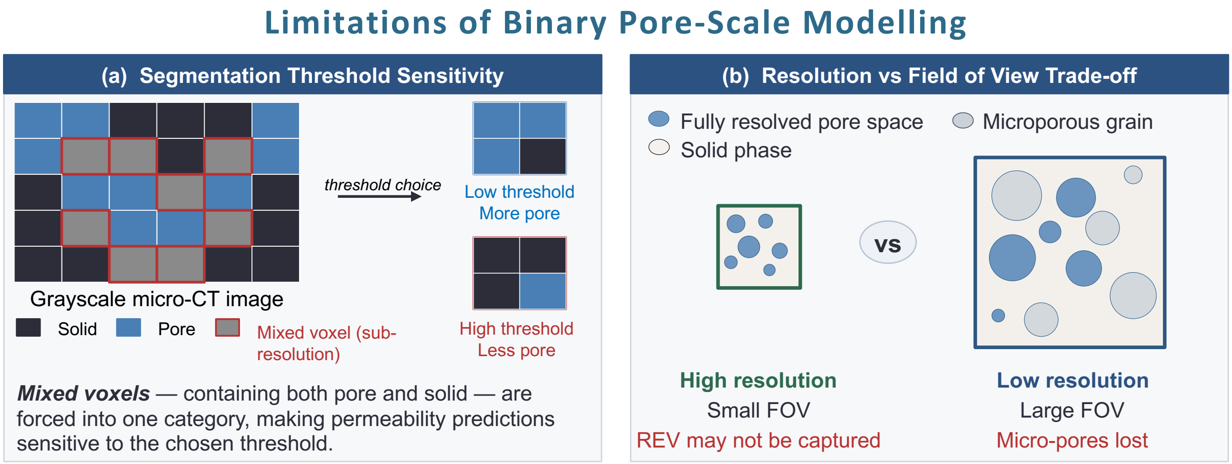

Fig. 1. Fundamental limitations of binary pore-scale modelling. (a) Segmentation threshold sensitivity. (b) Resolution vs. field-of-view trade-off.

in how the sub-voxel resistance is parameterised and in the macroscopic equations they recover.

Despite these advances, several aspects of the Guo greyscale LBM framework [13] remain incompletely addressed. The connection between this formulation and the classical Brinkman equation has not been derived within a single, self-consistent volume-averaging framework, and its behaviour under spatially varying porosity and permeability fields has not been analytically validated. In this work, we present a greyscale lattice Boltzmann framework for single-phase flow simulation on unsegmented micro-CT images of porous rock, formulated within the Guo approach. The framework couples the LBM solver with a Kozeny–Carman permeability closure calibrated from high-resolution binary sub-volume simulations, and is validated from analytical benchmarks through to sandstone images.

2 Greyscale Lattice Boltzmann Formulation

Single-phase flow is simulated using a D3Q19 lattice Boltzmann method (LBM) extended to porous media following the framework of [13]. Each voxel is characterised by a continuous porosity $\varepsilon \in (0,1]$ and an intrinsic permeability $k > 0$, allowing the solver to operate directly on unsegmented greyscale images without binary classification.

The sub-voxel flow resistance is incorporated through a porous drag force added to the collision step, which modifies the macroscopic momentum balance to recover the Darcy–Brinkman equation (derived in Section 3). The Darcy-scale velocity is recovered from the raw lattice momentum via the nonlinear closure of [13], which accounts for both viscous (Brinkman) and inertial (Forchheimer) drag. The MRT (Multiple-Relaxation-Time) collision operators is used, preferred for its numerical stability in heterogeneous domains.

Once steady state is reached, the bulk absolute permeability is extracted directly from Darcy's law:

$$K = \frac{\mu u_s}{\nabla p} \tag{1}$$

where u_s is the superficial velocity and ∇p is the applied pressure gradient. The porosity weighting internal to the solver cancels in this macroscopic flux–force relation, so the unscaled physical pressure gradient is used directly.

3 Analytical Validation: Homogeneous Porosity

Before applying the greyscale LBM to complex rock geometries, it is necessary to establish that the framework recovers the governing physics under controlled conditions. Section 3.1 derives analytically that the Guo formulation reduces to the classical Darcy–Brinkman equation under homogeneous porosity, which justifies using it as the macroscopic momentum model. Section 3.2 then provides numerical verification of this derivation using the parallel-plate benchmark, where exact analytical solutions exist for both the free-fluid and porous regimes. Agreement here confirms that discretisation, boundary conditions, and the collision operator are all implemented correctly before any rock geometry is introduced.

3.1 Theoretical Derivation of Darcy–Brinkman Equation

Flow in porous media can be rigorously described by volume averaging the Navier–Stokes equations over a representative elementary volume (REV). For single-phase incompressible flow, the volume-averaged momentum equation expressed in terms of the superficial velocity $\mathbf{u_s}$ takes the generalized Darcy–Brinkman form [13, 17]:

$$\frac{\partial \mathbf{u_s}}{\partial t} + (\mathbf{u_s}\cdot\nabla)\left(\frac{\mathbf{u_s}}{\varepsilon}\right) = -\frac{1}{\rho}\nabla(\varepsilon p) + \nu_e \nabla^2 \mathbf{u_s} - \varepsilon\frac{\nu_e}{k}\mathbf{u_s} + \varepsilon\mathbf{F}, \tag{2}$$

where $\varepsilon(\mathbf{x}) \in (0,1]$ is porosity, $k(\mathbf{x})$ is intrinsic permeability, ν_e is the effective kinematic viscosity, p is intrinsic pressure, $\mathbf{F}$ is body force per unit mass, and ρ is density. This form of the momentum equation arises from averaging over the total REV volume using the superficial velocity as the macroscopic flow variable. Under this convention, the pressure gradient appears as $\nabla(\varepsilon p)$ and the body force as $\varepsilon\mathbf{F}$ both weighted by porosity because only a fraction of the REV transmits momentum. We note that alternative averaging conventions exist, for example, averaging per fluid volume rather than total volume [18], which naturally yield ∇p as the driving force term with correspondingly different closure assumptions. The formulation presented here follows the superficial velocity convention of [13].

For steady-state creeping flow, we neglect the inertial term $(\mathbf{u}\cdot\nabla)(\mathbf{u}/\varepsilon)$ therefore Eq. (2) reduces to:

$$0 = -\nabla(\varepsilon p) + \mu_e \nabla^2 \mathbf{u}_s - \varepsilon \frac{\mu_e}{k}\mathbf{u}_s + \varepsilon\rho\mathbf{F}, \quad (3)$$

where $\mu_e = \rho\nu_e$ is the effective dynamic viscosity. Applying the product rule, $\nabla(\varepsilon p) = \varepsilon\nabla p + p\nabla\varepsilon$, and assuming homogeneous porosity $\nabla\varepsilon = 0$, Eq. (3) simplifies to:

$$0 = -\varepsilon\nabla p + \mu_e \nabla^2 \mathbf{u}_s - \frac{\varepsilon\mu_e}{k}\mathbf{u}_s + \varepsilon\rho\mathbf{F}. \quad (4)$$

Dividing by ε,

$$0 = -\nabla p + \frac{\mu_e}{\varepsilon}\nabla^2 \mathbf{u}_s - \frac{\mu_e}{k}\mathbf{u}_s + \rho\mathbf{F}. \quad (5)$$

Eq. (5) is identical in structure to Brinkman's modification of Darcy's law [19],

$$\nabla p = -\frac{\mu}{k}\mathbf{u_s} + \mu'\nabla^2\mathbf{u_s}, \quad (6)$$

where Brinkman introduced the viscosity parameter μ' to represent viscous stress transport in porous media and explicitly noted that it may differ from the fluid viscosity [19]. Within the superficial velocity averaging convention adopted here, comparison of Eq. (5) and (6) shows that the Brinkman viscosity parameter μ' maps to μ_e/ε. This mapping is a consequence of the chosen averaging framework rather than a universal result; formulations based on different averaging conventions may recover different expressions for the effective viscosity parameter [18].

This result demonstrates that porosity directly modifies viscous momentum diffusion even when the porosity is spatially uniform. The classical Darcy–Brinkman equation expressed in superficial velocity form is therefore

$$-\nabla p + \frac{\mu_e}{\varepsilon}\nabla^2 \mathbf{u}_s - \frac{\mu_e}{k}\mathbf{u}_s + \rho\mathbf{F} = 0. \quad (7)$$

While the superficial velocity represents the volumetric flux per unit total area, resulting in a physically meaningful velocity within the fluid phase as the intrinsic phase average velocity. [20] demonstrated using volume averaging theory that intrinsic velocity provides an appropriate macroscopic variable for describing momentum transport in porous media.

The Darcy–Brinkman equation expressed in intrinsic phase average velocity ($\mathbf{u_s} = \varepsilon\mathbf{u_i}$) form is therefore

$$-\nabla p + \mu_e\nabla^2\mathbf{u}_i - \frac{\mu_e}{k_B}\mathbf{u}_i + \rho\mathbf{F} = 0, \qquad k_B = \frac{k}{\varepsilon}. \quad (8)$$

Within the REV-volume averaging convention, this derivation shows how the Guo formulation connects to the Brinkman equation and yields the permeability mapping $k_B = k/\varepsilon$ as a direct consequence of the intrinsic–superficial velocity transformation. When expressed in superficial velocity form, porosity enters as a modifier of the effective viscosity; when expressed in intrinsic velocity form, it enters as a modifier of the effective permeability.

3.2 Analytical Solution and Validation of The Greyscale LBM Formulation

We consider steady, fully developed flow between two infinite parallel plates separated by distance $2h$. The flow is unidirectional, with velocity depending only on the transverse coordinate, and is driven by a constant pressure gradient or equivalently a uniform body force. This configuration provides exact analytical solutions in both free-fluid and porous regimes and therefore serves as a rigorous benchmark for verifying recovery of the Navier–Stokes and Darcy–Brinkman under homogeneous porosity, as well as the permeability scaling relation $k_B = k/\varepsilon$ established in Eq. 8.

3.2.1 Analytical Solution

In the absence of porous drag, the governing equation reduces to the steady Stokes equation,

$$\mu_e\frac{d^2u}{dy^2} + \rho F = 0, \quad (9)$$

where the applied body force incorporates the pressure gradient according to

$$\rho F = -\frac{dp}{dz}. \quad (10)$$

Applying no-slip boundary conditions at $y = \pm h$ yields the classical Poiseuille solution,

$$u(y) = \frac{\rho F}{2\mu_e}\left(h^2 - y^2\right), \quad (11)$$

with cross-sectional mean velocity

$$\bar{u} = \frac{\rho F h^2}{3\mu_e}. \quad (12)$$

This solution provides the reference free-fluid limit corresponding to vanishing porous resistance.

For flow in a porous medium, the intrinsic phase average velocity satisfies the Darcy–Brinkman equation (Eq. 8) derived in Section 3.1.

$$\mu_e\frac{d^2u_i}{dy^2} - \frac{\mu_e}{k_B}u_i + \rho F = 0. \quad (13)$$

The solution satisfying symmetry at the channel centerline and no-slip boundary conditions at the walls is

$$u_i(y) = \frac{\rho F k_B}{\mu_e}\left[1 - \frac{\cosh\left(y/\sqrt{k_B}\right)}{\cosh\left(h/\sqrt{k_B}\right)}\right]. \quad (14)$$

The corresponding mean intrinsic velocity is

$$\bar{u}_i = \frac{\rho F k_B}{\mu_e}\left[1 - \frac{\sqrt{k_B}}{h}\tanh\left(\frac{h}{\sqrt{k_B}}\right)\right]. \tag{15}$$

The free-fluid solution (Eq. 12) is recovered asymptotically as $k_B \to \infty$, confirming consistency with the Navier–Stokes limit.

The Greyscale LBM model recovers the macroscopic momentum equation in superficial velocity form (Eq. 3). For steady fully developed flow, the governing equation reduces to

$$\nu_e \frac{d^2 u_s}{dy^2} - \frac{\varepsilon \nu_e}{k} u_s + \varepsilon F = 0. \tag{16}$$

Using the intrinsic–superficial velocity relation (Eq. **??**), Eq. (16) becomes identical to the Darcy–Brinkman (Eq. 13) when the permeability scaling $k_B = k/\varepsilon$ is applied. The analytical mean superficial velocity is therefore

$$\bar{u}_s = \frac{kF}{\nu_e}\left[1 - \frac{\sqrt{k/\varepsilon}}{h}\tanh\left(\frac{h}{\sqrt{k/\varepsilon}}\right)\right]. \tag{17}$$

This result demonstrates analytically that the Greyscale LBM formulation recovers the Darcy–Brinkman equation exactly and confirms that permeability scaling arises directly from the intrinsic–superficial velocity transformation derived in Section 3.1.

3.2.2 Numerical validation

Section 3.2.1 established closed-form analytical expressions for the mean velocity in both free-fluid and porous regimes. Since the mean superficial velocity uniquely characterizes the macroscopic flux under fully developed conditions, quantitative agreement between the analytical predictions and numerical LBM results provides a direct validation of the recovered macroscopic momentum equation. To verify this correspondence, numerical simulations were performed for steady, fully developed flow between two infinite parallel plates, corresponding to the analytical configuration. The computational domain, as illustrated in Fig. 2, consisted of a three-dimensional lattice of size $(N_x, N_y, N_z) = (100, 100, 200)$ with no-slip boundary conditions imposed at the channel walls $y = \pm h$ and periodic boundary conditions applied in the streamwise and spanwise directions. The half-channel height was defined as

$$h = \frac{N_y - 2}{2}. \tag{18}$$

Flow was driven by a uniform body force $\mathbf{F} = (0, 0, F)$, equivalent to a constant pressure gradient. The forcing magnitude was chosen such that the maximum velocity satisfied $u_{\max} \lesssim 0.05$, ensuring creeping-flow conditions. Simulations were conducted for both the free-fluid limit and a porous medium with intrinsic permeability $k = 100$ Darcy and $\varepsilon = 0.5$, corresponding to a Brinkman permeability $k_B = k/\varepsilon = 200$ Darcy, as required by the analytical mapping derived in Section 3.1 and recovered in Section 3.2.1. The density and effective relaxation time were set to $\rho = 1$, and $\tau_{\text{eff}} = 0.7$ in lattice units, respectively, representative of a water-like fluid in the Stokes flow regime.

Fig. 3 compares the analytical and numerical mean superficial velocities for both free-fluid and porous cases. All data collapse onto the one-to-one correspondence line, demonstrating that the numerical solution recovers the analytical prediction with negligible error.

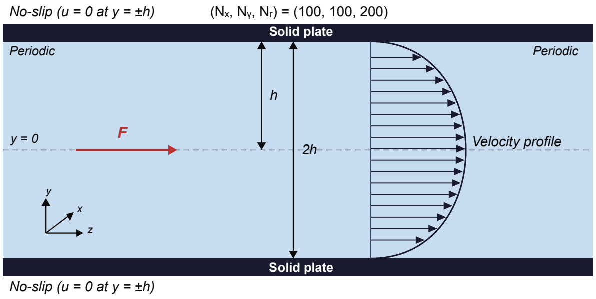

Fig. 2. Computational domain for the parallel-plate benchmark. A three-dimensional lattice of size $(N_x, N_y, N_z) = (100, 100, 200)$ with no-slip boundary conditions at the channel walls, periodic conditions in the streamwise and spanwise directions, and a uniform body force F driving flow along the Z-axis.

Having confirmed that the greyscale LBM recovers the correct macroscopic behaviour under homogeneous porosity conditions, we now turn to spatially varying porosity fields where analytical and numerical benchmarks of increasing complexity are used to validate the heterogeneous extension of the model.

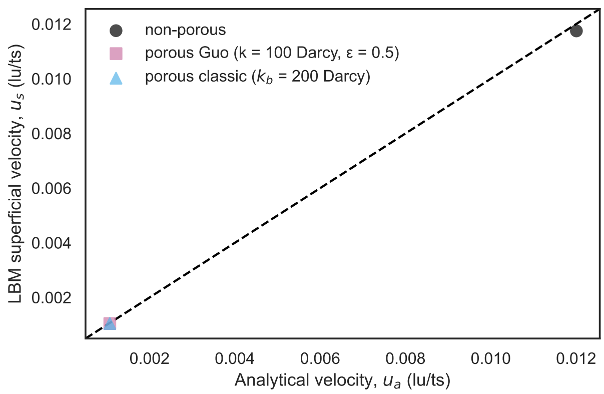

Fig. 3. Parity plot of analytical and LBM superficial velocities for free-fluid and porous cases, confirming quantitative recovery of the Darcy–Brinkman equation.

4 Heterogeneous Porosity

This section extends the validation to heterogeneous porosity fields through three cases of increasing complexity. First, a linear porosity and permeability gradient is used to derive and verify an exact analytical solution for bulk permeability within the Guo framework. Second, a coarsened binary image of Bentheimer sandstone provides a controlled test on a realistic pore geometry where the greyscale field is constructed by spatial averaging of a known resolved structure. Third, a greyscale micro-CT image of

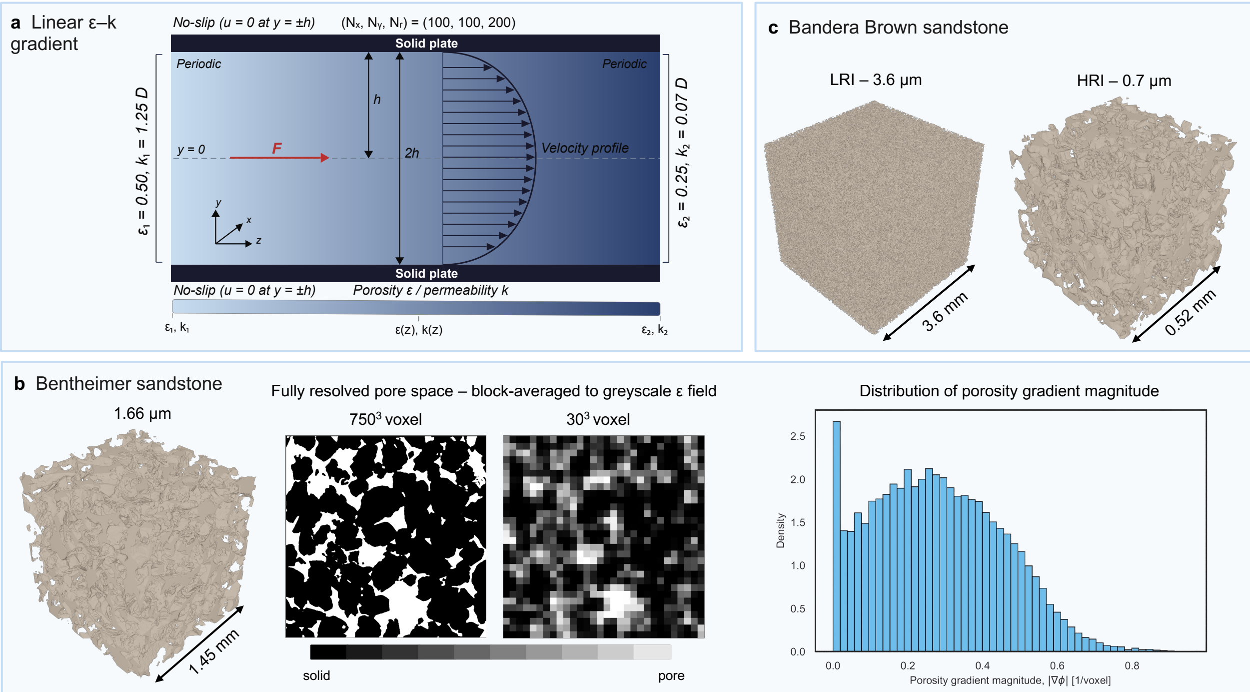

Fig. 4. Computational domains for the three heterogeneous porosity validation cases. (a) linear ε–k gradient: a parallel-plate with porosity and intrinsic permeability varying linearly along the flow direction. (b) Bentheimer sandstone: a high-resolution binary pore space block-averaged to a coarsened greyscale porosity field, with the porosity gradient magnitude histogram confirming significant spatial heterogeneity concentrated between 0.1 and 0.5 $voxel^{-1}$ (c) Bandera Brown sandstone: micro-CT images acquired at two resolutions–a low-resolution greyscale image covering a large field of view and a high-resolution binary image of a co-registered sub-volume.

Bandera Brown sandstone, in which intermediate intensities arise from physically unresolved microporosity, serves as the most demanding validation case and is used to assess resolution sensitivity of the method. This case also forms the basis for a complete greyscale simulation workflow, from image acquisition and porosity mapping to permeability calibration and prediction. Fig. 4 demonstrates the computational domains used in this section.

4.1 Linear Porosity and Permeability Gradient

We construct a controlled benchmark in which both the porosity and intrinsic permeability vary linearly along the flow direction. This configuration admits an exact analytical solution for the bulk absolute permeability within the Guo framework and therefore provides a rigorous test of the model's ability to handle porosity gradients. The computational domain follows the same configuration as Section 3.2.2, a three-dimensional lattice of size $(N_x, N_y, N_z) = (100, 100, 200)$. The porosity field is prescribed as a linear ramp along Z:

$$\varepsilon(z) = \varepsilon_1 + (\varepsilon_2 - \varepsilon_1)\frac{z}{L}, \qquad z \in [0, L], \tag{19}$$

where $L = 200$ voxels. Two gradient configurations are examined: a decreasing gradient with $(\varepsilon_1, \varepsilon_2) = (0.5, 0.25)$ and an increasing gradient with $(\varepsilon_1, \varepsilon_2) = (0.25, 0.5)$. The intrinsic permeability field is assigned through a linear k–ε relationship,

$$k(z) = k_1 + (k_2 - k_1)\frac{\varepsilon(z) - \varepsilon_1}{\varepsilon_2 - \varepsilon_1}, \tag{20}$$

with anchor values $k_1 = 0.0694$ Darcy at $\varepsilon_1 = 0.25$ and $k_2 = 1.25$ Darcy at $\varepsilon_2 = 0.5$, so that permeability and porosity are co-directional along Z in both cases.

For steady creeping flow driven by a uniform body force F under periodic boundary conditions, and setting $\rho = 1$ in lattice units, Eq. (3) reduces to:

$$\frac{d(\varepsilon p)}{dz} = \varepsilon\left(F - \frac{\mu u_s}{k}\right). \tag{21}$$

Continuity requires $u_s =$ const along Z. In the Guo model the pressure is defined as $p = c_s^2\rho/\varepsilon$, so $\varepsilon p = \rho c_s^2$. For incompressible flow ρ is spatially uniform, hence $[\varepsilon p]_0^L = 0$. Integrating Eq. (21) over the domain length L and applying this condition yields:

$$0 = F\int_0^L \varepsilon(z)\,dz - \mu\,u_s\int_0^L \frac{\varepsilon(z)}{k(z)}\,dz. \tag{22}$$

Solving for u_s:

$$u_s = \frac{\displaystyle\int_0^L \varepsilon(z)\,dz}{\displaystyle\int_0^L \varepsilon(z)/k(z)\,dz}, \tag{23}$$

by knowing $\langle\cdot\rangle = L^{-1}\int_0^L(\cdot)dz$ and comparing with

Darcy's law (Eq. 1), the bulk absolute permeability is:

$$K = \frac{\langle \varepsilon \rangle}{\langle \varepsilon/k \rangle} = \frac{L^{-1}\int_0^L \varepsilon(z)\,dz}{L^{-1}\int_0^L \varepsilon(z)/k(z)\,dz}. \quad (24)$$

Evaluating the integrals analytically, $\langle \varepsilon \rangle = (\varepsilon_1 + \varepsilon_2)/2 = 0.375$. For the denominator, a change of variable $z \to \varepsilon$ gives:

$$\langle \varepsilon/k \rangle = \frac{1}{\varepsilon_2 - \varepsilon_1}\int_{\varepsilon_1}^{\varepsilon_2} \frac{\varepsilon}{k(\varepsilon)}\,d\varepsilon. \quad (25)$$

With $k(\varepsilon) = a\varepsilon + b$, where $a = (k_2 - k_1)/(\varepsilon_2 - \varepsilon_1) = 4.722$ and $b = k_1 - a\varepsilon_1 = -1.111$, the antiderivative $\int \varepsilon/(a\varepsilon + b)\,d\varepsilon = \varepsilon/a - (b/a^2)\ln|a\varepsilon + b|$ yields $\langle \varepsilon/k \rangle = 0.7877$, and the analytical bulk absolute permeability is:

$$K_{\text{analytical}} = \frac{0.375}{0.7877} = 0.4760 \text{ Darcy}. \quad (26)$$

This result can be compared against the classical, series-average permeability. For incompressible flow through layers in series, conservation of volumetric flux alone (with no porosity weighting) requires the local pressure gradient in each layer to satisfy Darcy's law $-dp/dz = \mu u_s/k(z)$, where u_s is the same constant flux through every cross-section. Integrating directly gives the classical harmonic average

$$K_h = \frac{1}{\langle 1/k \rangle} = \frac{L}{\int_0^L dz/k(z)}. \quad (27)$$

Evaluating Eq. (27) for the linear profile $k(z) = k_1 + (k_2 - k_1)z/L$ gives the closed-form result

$$K_h = \frac{k_2 - k_1}{\ln(k_2/k_1)} = \frac{1.25 - 0.0694}{\ln(1.25/0.0694)} = 0.4084 \text{ Darcy}. \quad (28)$$

LBM simulations were performed for both gradient orientations: for the decreasing gradient (ε: $0.5 \to 0.25$), $K = 0.4893$ Darcy, and for the increasing gradient (ε: $0.25 \to 0.5$) an identical value of $K = 0.4893$ Darcy is obtained. The identical result for both gradient directions is physically required, the bulk permeability of a series arrangement is independent of orientation, and confirms that the Guo formulation handles the $\nabla(\varepsilon p)$ coupling symmetrically for positive and negative porosity gradients alike.

The LBM result and $K_{\text{analytical}}$ agree with eachother to within 2.8%, confirming that the LBM correctly solves the Guo model's own governing equations. However, both deviate from the physically correct harmonic average K_h (Eq. 28) by 16–20%. This reveals a limitation of the Guo formulation rather than a numerical artefact: the $\nabla(\varepsilon p)$ driving term in Eq. (2) couples the macroscopic pressure balance to the local porosity gradient through the $p\nabla\varepsilon$ term, biasing the predicted bulk permeability away from the true series average whenever porosity varies along the flow direction.

4.2 Coarsened Bentheimer Sandstone

To extend the validation beyond analytically tractable configurations, we apply the greyscale LBM to a coarsened micro-CT image of a sandstone rock sample. This case serves as an intermediate benchmark between the linear gradient and the full greyscale rock image, testing the ε-weighted integration scheme under realistic, non-monotonic porosity heterogeneity. A high-resolution segmented pore geometry was coarsened into a greyscale representation using block averaging, yielding a spatially varying porosity field $\varepsilon(\mathbf{x})$. Voxels with $\varepsilon = 0$ were treated as impermeable solids, while the remaining voxels formed a connected flow domain. Fig. 4b illustrates the correspondence between the fully resolved pore space and the upscaled porosity field, demonstrating how unresolved pore-scale heterogeneity is represented as a continuous porosity distribution. Closure of the macroscopic momentum equation in the greyscale domain requires specification of an intrinsic permeability field $k(\mathbf{x})$. This was obtained using a Kozeny–Carman–type relationship,

$$k(\varepsilon) = C\frac{\varepsilon^3}{(1-\varepsilon)^2}, \quad (29)$$

where C is a geometric constant and was obtained from single-phase LBM simulations performed on representative binary subdomains. To construct the calibration dataset, representative binary sub-blocks were extracted from the fully resolved pore space of the Bentheimer image. The coarsened porosity map was scanned and, for each of the nine target porosity levels $\phi \in \{0.1, 0.2, \ldots, 0.9\}$, up to five blocks whose block-averaged porosity lay within a tolerance of ± 0.02 of the target were selected. Each selected block retains the original binary segmentation at $1.66\,\mu$m resolution, so that the pore geometry is fully resolved within it. To ensure hydraulic connectivity, only blocks in which the pore phase percolated continuously along the primary flow direction were accepted. A binary LBM simulation was then performed on each accepted block and the block-scale intrinsic permeability k_i was extracted at steady state via Darcy's law (Eq. 1).

The fitting results are shown in Fig. 5. The left panel presents the measured permeability–porosity pairs together with the fitted Kozeny–Carman relationship. To obtain a robust estimate of C, each measurement was transformed into an implied constant,

$$C_i = \frac{k_i}{\varepsilon_i^3/(1-\varepsilon_i)^2}. \quad (30)$$

The right panel of Fig. 5 shows the distribution of these implied constants as a function of porosity. The final C was obtained using a robust binning procedure with outlier rejection based on the interquartile range, followed by aggregation using a weighted median.

Using the generated permeability field, the greyscale LBM predicts an absolute permeability of 1.68 Darcy against a reference of 1.81 Darcy, corresponding to a 7.71% relative difference. The porosity gradient magnitude histogram (Fig. 4b) confirms that significant spatial heterogeneity is present in the coarsened domain, with most gradients concentrated between 0.1 and 0.5 $voxel^{-1}$. Furthermore, the 7.71% relative difference confirms that the Kozeny–Carman parameterisation, despite its simplicity,

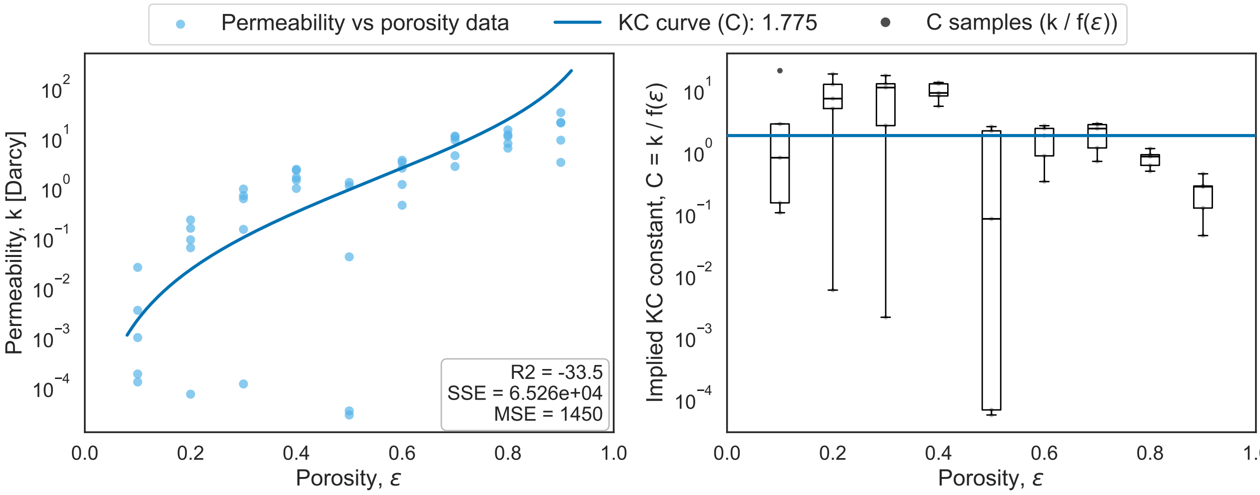

Fig. 5. Kozeny–Carman permeability–porosity calibration for coarsened Bentheimer sandstone. Left: fitted KC curve (C = 1.775). Right: distribution of implied constants used for robust estimation of C.

provides a sufficient closure for the intrinsic permeability field.

This result is notable in light of the bias identified in the linear-gradient benchmark (Section **??**): although the local porosity gradient magnitude in the coarsened Bentheimer domain is roughly two to three orders of magnitude larger than in the linear case ($|\nabla\varepsilon| = (\varepsilon_2 - \varepsilon_1)/L = 0.25/200 = 1.25 \times 10^{-3}\,\text{voxel}^{-1}$), the resulting greyscale permeability error (7.71%) is substantially smaller than the 16–20% bias found in the linear benchmark. The difference is explained by the direction of the porosity gradient relative to flow rather than its magnitude. In the linear benchmark, $\nabla\varepsilon$ is monotonic and exactly co-directional with the macroscopic flow over the full domain length, so the $p\nabla\varepsilon$ bias term in Eq. 2 accumulates coherently and never cancels. In the coarsened sandstone, $\nabla\varepsilon$ varies in orientation throughout the connected pore network relative to the locally tortuous flow paths, so the bias term takes both signs across the domain and largely cancels when integrated over the full three-dimensional geometry. The linear benchmark therefore represents a worst-case configuration for this bias, while realistic porous media, where porosity gradients are locally large but directionally incoherent with respect to flow, are far less susceptible to it.

The scatter in the implied KC constant in Fig. 5 reflects genuine variability in pore geometry that a single scalar C cannot capture: at any given porosity, sub-blocks drawn from different regions of the sandstone will differ in grain shape, pore throat distribution, and connectivity, all of which influence permeability independently of porosity. The Kozeny–Carman relation conflates these geometric differences into a single parameter, so the implied C values spread across nearly two orders of magnitude at intermediate porosities. Despite this, the bulk permeability prediction remains within 7.71% of the binary reference. This agreement arises because the simulation integrates the permeability field over the entire domain: spatial averaging across many voxels suppresses the local errors introduced by assigning a constant C, provided the scatter is approximately symmetric about the median. The use of a robust weighted-median estimator for C, combined with interquartile-range outlier rejection, ensures that the assigned constant reflects the central tendency of the distribution rather than being biased by geometric outliers at extreme porosities.

4.3 Bandera Brown Sandstone

Unlike the Bentheimer case in Section 4.2, where a greyscale domain was constructed synthetically by block-averaging a resolved binary image, the Bandera Brown sandstone provides a more demanding test: a greyscale micro-CT image in which intermediate intensities arise physically from unresolved micropores rather than from spatial averaging of a known geometry. This distinction is important because the sub-voxel pore structure is not accessible from the greyscale image alone and must be characterised independently. The validation therefore requires two images of the same physical sample acquired at different resolutions, a high-resolution binary reference and a low-resolution greyscale image, combined through three-dimensional co-registration.

4.3.1 Image Acquisition

Two micro-CT images of the same Bandera Brown sandstone core were acquired using Micro-Computed Tomography (MCT) beamline at the Australian Synchrotron ANSTO: the high-resolution image (HRI) at 9× magnification with a voxel size of 0.7 μm, and the low-resolution image (LRI) at 1.8× magnification with a voxel size of 3.6 μm with a field of view approximately five times larger in each linear dimension. The HRI was segmented into a binary pore-solid geometry using hysteresis thresholding, while the LRI image was retained in greyscale form for use in the greyscale LBM workflow.

To compare permeability predictions from the two images on the same physical rock region, a three-dimensional rigid co-registration was performed. The HRI binary volume served as the fixed image and the LRI greyscale volume as the moving image. Following registration, a sub-volume of the LRI image spatially coincident with the HRI field of view was extracted by applying the recovered transformation and resampling onto the HRI coordinate frame at 3.6 µm voxel size.

4.3.2 Porosity and Permeability Maps

The greyscale intensity field of the LRI image was converted to a voxel-level porosity map using histogram-based peak detection. Two dominant peaks were identified in the smoothed intensity histogram: a low-intensity peak corresponding to macropore space (I_{pore}) and a high-intensity peak corresponding to solid grains (I_{solid}). Voxels with intermediate intensities, arising from unresolved micropores where pore size falls below the 3.6 μm voxel resolution, were assigned a sub-voxel porosity through the linear mapping

$$\phi_0 = \text{clip}\left(\frac{I_{\text{solid}} - I}{I_{\text{solid}} - I_{\text{pore}}}, 0, 1\right), \tag{31}$$

so that $I \leq I_{\text{pore}}$ gives $\phi_0 = 1$ (macropore) and $I \geq I_{\text{solid}}$ gives $\phi_0 = 0$ (solid). The resulting porosity map served as the input to both the KC permeability assignment and the greyscale LBM simulation.

The intrinsic permeability field was assigned through the Kozeny-Carman relationship (Eq. 29), with the geometric constant C calibrated from pore-scale LBM simulations on binary sub-cubes extracted from the segmented HRI image, following the same procedure as Section 4.2. Sub-cube extraction was performed by evaluating 20,000 randomly placed candidate positions within the HRI binary volume. Each candidate was a 50^3 voxel cube and was accepted only if (i) the pore phase percolated along the Z direction and (ii) the isolated pore fraction did not exceed 10%. For each of the nine target porosity levels $\phi \in \{0.1, 0.2, \ldots, 0.9\}$, the five best-matching accepted candidates were selected. The 50^3 voxel cube was chosen to balance two competing requirements: blocks must be large enough to capture representative pore geometry, yet small enough that the rock's natural spatial variability provides samples spanning the full target porosity range, since larger sub-cubes progressively average out local heterogeneity, making it impossible to find blocks at the extreme ends of the porosity range. The resulting calibration data and fitted curve are shown in Fig. 6 giving $C = 2.67\,\mu\text{m}^2$.

4.3.3 Permeability Comparison: Greyscale vs Binary

To validate the greyscale workflow, simulations were compared on the co-registered sub-volume where both the HRI binary and LRI greyscale images represent the same physical rock region. Binary LBM on the 0.7 μm HRI sub-volume yielded $k = 423$ mD, serving as the reference. Greyscale LBM on the 3.6 μm co-registered LRI sub-volume with the calibrated C yielded $k = 427$ mD, a relative difference of approximately 1%. This close agreement demonstrates that the greyscale framework, combined with the KC permeability assignment calibrated from the high-resolution image, accurately reproduces the pore-scale reference despite operating at a voxel size five times coarser.

Having validated the method on the co-registered sub-volume, greyscale LBM was applied to the full LRI domain (3.6 mm cubed) to quantify the contribution of microporosity to the effective permeability. For comparison, a binary segmentation of the same LRI image was also simulated, in which all grey voxels were classified as open pore space. The binary simulation yielded $k = 500$ mD, while the greyscale simulation yielded $k = 259$ mD, a difference of approximately 93%. This large discrepancy demonstrates that grey voxels in the 3.6 μm image impose significant flow resistance that is entirely absent from the binary representation.

This observation motivates the calibration workflow illustrated in Fig. 7. When a low-resolution greyscale image is available alongside a high-resolution binary image of the same rock, C at the target resolution can be estimated.

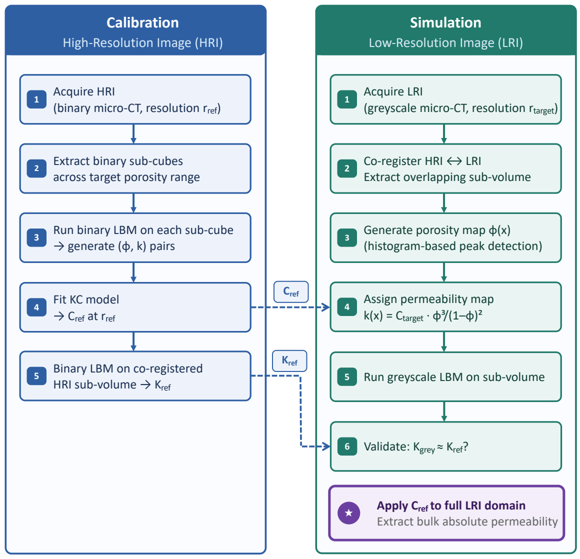

Fig. 7. Greyscale LBM framework for permeability prediction: KC calibration from high-resolution binary simulations (left), and permeability prediction on the low-resolution greyscale domain (right).

4.3.4 Resolution Sensitivity of Kozeny–Carman Constant

A practically important question is what happens when C calibrated at one resolution is applied to an image acquired at a substantially different resolution. A common scenario when only a single greyscale image is available and co-registration is not possible. To quantify this, we coarsened the 3.6 μm HRI image by block-averaging at factors of 2×, 4×, 6×, and 8×, yielding effective voxel sizes of 7.2, 14.4, 21.6, and 28.8 μm. At each resolution, the porosity map was regenerated from the coarsened intensity field. Rather than applying the original $C = 2.67\ \mu\text{m}^2$ directly, the value of C required to recover the baseline greyscale LBM permeability of 259mD was determined at each resolution. The results are summarized in Table 1.

When C is held fixed at 2.67 μm^2, the predicted per-

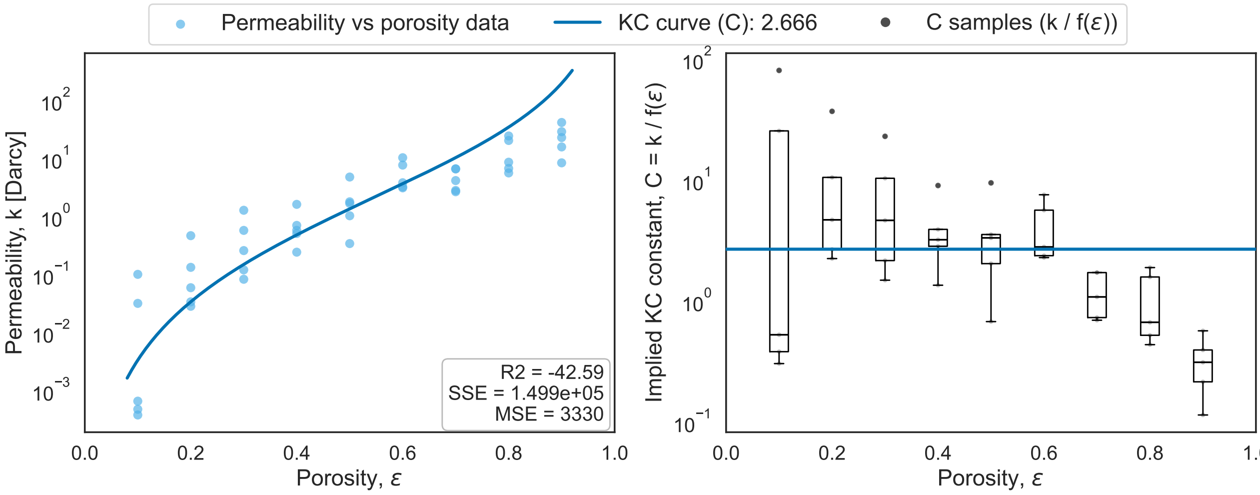

Fig. 6. Kozeny–Carman calibration from binary LBM simulations on 50^3 voxel sub-cubes of the Bandera Brown HRI. Left: fitted KC curve (C = 2.67 μm). Right: implied constants used for robust estimation of C.

Table 1. Value of the KC constant C required to recover the baseline permeability of 259 mD as a function of effective resolution.

Coarsen factor	Effective resolution (μm)	Porosity	k at C = 2.67 μm^2 (mD)	C to match 259 mD (μm^2)
1× (baseline)	3.6	0.207	259	2.67
2×	7.2	0.208	288	2.30
4×	14.4	0.213	380	1.35
6×	21.6	0.221	531	0.70
8×	28.8	0.228	677	0.44

meability increases monotonically with voxel size, reaching 677 mD at 28.8 μm, a 161% overestimation relative to the 3.6 μm baseline. This trend arises because block-averaging smears sharp solid–pore interfaces into intermediate grey voxels that are then assigned non-zero Darcy permeability through the KC relation, Second, the non-linear KC mapping amplifies even modest increases in apparent porosity into disproportionately large increases in local permeability. The required C therefore falls from 2.67 μm^2 at 3.6 μm to 0.44 μm^2 at 28.8 μm, a reduction of 83%.

Fig. 8 shows this decrease in C with resolution. Although the relationship appears nonlinear in C, the right panel of Fig. 8 reveals that $\sqrt{C}$ varies linearly with effective resolution r. This linearity shows that C is resolution-dependent for greyscale images and cannot be treated as a universal rock constant independent of imaging conditions. Practitioners who lack co-registered multi resolution images and must transfer C across a large resolution gap should expect systematic permeability overestimation, the magnitude of which grows rapidly with the resolution difference. The linear $\sqrt{C}$ relationship provides a practical means of estimating the appropriate C at any target resolution from a small number of coarsened images of the HRI, without requiring additional experimental acquisitions.

As Table 1 shows, bulk porosity is nearly conserved under coarsening, yet the predicted permeability at fixed C nearly triples. The driver is therefore not mean porosity but the shape of the porosity field. Block-averaging acts as a low-pass filter on $\varepsilon(\mathbf{x})$, and permeability is bottleneck-controlled, set by the lowest-porosity voxels along the percolating path. Because the Kozeny-Carman function (Eq. 29) increases nonlinearly with porosity, smearing a tight throat upward by mixing in adjacent higher-porosity material moves that voxel into a steeper region of $k(\varepsilon)$, causing a disproportionate jump in local permeability, collapsing the dominant flow resistance and inflating K. C must therefore fall to compensate. The magnitude of this effect is governed by the local porosity contrast $\Delta\varepsilon = \varepsilon_b - \varepsilon_t$ between throat and adjacent pore body: larger contrast means greater sensitivity to coarsening, and the linear $\sqrt{C}$–resolution trend reflects how this throat smearing accumulates proportionally with voxel size. It should be noted that the magnitude of this effect is rock-specific, depending on the spatial arrangement of porosity within the image.

5 Conclusions

We have presented a greyscale lattice Boltzmann framework for single-phase flow simulation on unsegmented micro-CT images of porous rock. By assigning each voxel a continuous porosity and a Kozeny–Carman permeability closure, the framework bypasses the segmentation step that underlies conventional pore-scale modelling and its associated uncertainties. Analytical derivation confirms recovery of the Darcy–Brinkman equation under homogeneous porosity, and validation against exact and numerical benchmarks demonstrates correct handling of heterogeneous porosity and permeability fields. Applied to Bandera Brown sandstone, the framework achieves 1% agreement with high-resolution binary simulations on a co-registered sub-volume, while full-domain comparisons re-

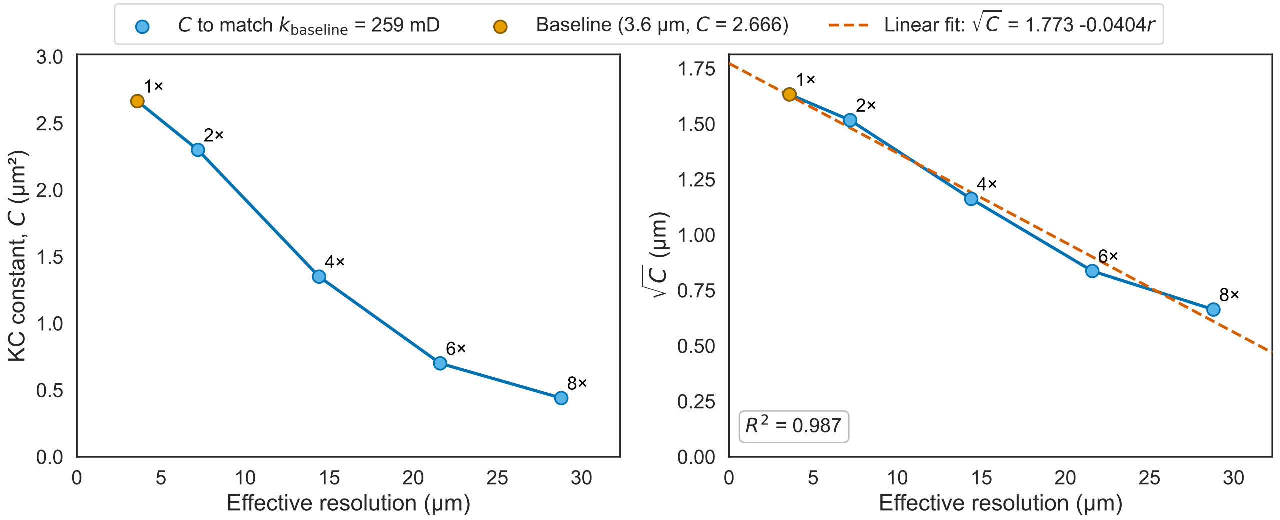

Fig. 8. Resolution dependence of the KC constant C (left) and $\sqrt{C}$ (right) for Bandera Brown sandstone. The linear scaling of $\sqrt{C}$ with voxel size ($R^2 = 0.987$) enables calibration at any target resolution.

veal a 93% divergence (which is resolution-dependent) between greyscale and binary predictions, demonstrating that microporosity imposes significant flow resistance entirely absent from binary representations. Therefore, binary segmentation, by ignoring microporous flow resistance, would systematically bias multiphase flow predictions, with errors propagating directly into field-scale upscaling workflows. Finally, we established that the Kozeny-Carman constant C is intrinsically resolution-dependent, with $\sqrt{C}$ scaling linearly with voxel size, providing a practical calibration route when co-registered multi-resolution images are unavailable. We also identified an intrinsic limitation of the Guo formulation, whereby spatially varying porosity introduces a bias in predicted permeability. This bias is largest when porosity gradients are coherently aligned with the flow direction, but largely cancels in the disordered pore networks of the sandstones studied here; further work is needed to assess its significance in rocks with persistent, flow-aligned porosity trends. Together, these results position greyscale simulation as a rigorous and computationally accessible tool for characterising fluid transport in rocks with multiscale porosity, where conventional binary approaches are most likely to fail.

The authors acknowledge the Micro-Computed Tomography (MCT) beamline at the Australian Synchrotron ANSTO. This research was conducted with the assistance of resources and services provided by the National Computational Infrastructure (NCI), supported by the Australian Government.

References

[1] D. Wildenschild and A. P. Sheppard, Advances in Water Resources, **51**, 217–246 (2013).

[2] M. J. Blunt, Multiphase Flow in Permeable Media: A Pore-Scale Perspective(Cambridge University Press, Cambridge, 2017).

[3] F. O. Alpak, F. Gray, N. Saxena, J. Dietderich, R. Hofmann, and S. Berg, Computational Geosciences, **22**, 815–832 (2018).

[4] J. E. McClure, Z. Li, M. Berrill, and T. Ramstad, Computational Geosciences, **25**, 871–895 (2021).

[5] A. Q. Raeini, M. J. Blunt, and B. Bijeljic, Advances in Water Resources, **74**, 116–126 (2014).

[6] S. Foroughi, M. J. Shojaei, N. Lane, B. Rashid, D. Lakshtanov, Y. Ning, Y. Zapata, B. Bijeljic, and M. J. Blunt, Transport in Porous Media, **152** (2025).

[7] N. Saxena, R. Hofmann, F. O. Alpak, J. Dietderich, S. Hunter, and R. J. Day-Stirrat, Marine and Petroleum Geology, **86**, 972–990 (2017).

[8] G. Garfi, C. M. John, S. Berg, and S. Krevor, Transport in Porous Media, **131**, 985–1005 (2019).

[9] M. F. Salek and L. E. Beckingham, Earth and Space Science, **10** (2023).

[10] P. Mostaghimi, M. J. Blunt, and B. Bijeljic, Mathematical Geosciences, **45**, 103–125 (2012).

[11] L. Zhang, B. Guo, C. Qin, and Y. Xiong, Advances in Water Resources, **190**, 104753 (2024).

[12] I. Nabipour, M. Mohammadzadeh-Shirazi, A. Raoof, and J. Qajar, Transport in Porous Media, **152** (2025).

[13] Z. Guo and T. S. Zhao, Physical Review E, **66** (2002).

[14] J. Zhu and J. Ma, Advances in Water Resources, **56**, 61–76 (2013).

[15] R. Li, Y. S. Yang, J. Pan, G. G. Pereira, J. A. Taylor, B. Clennell, and C. Zou, Physical Review E, **90** (2014).

[16] J. Zhu and J. Ma, Scientific Reports, **8** (2018).

[17] P. Nithiarasu, K. Seetharamu, and T. Sundararajan, International Journal of Heat and Mass Transfer, **40**, 3955–3967 (1997).

[18] C. Soulaine, Water Resources Research, **60** (2024).

[19] H. C. Brinkman, Flow, Turbulence and Combustion, **1** (1949).

[20] S. Whitaker, Transport in Porous Media, **1**, 3–25 (1986).